# NJC

Accepted Manuscript


This is an *Accepted Manuscript*, which has been through the Royal Society of Chemistry peer review process and has been accepted for publication.

*Accepted Manuscripts* are published online shortly after acceptance, before technical editing, formatting and proof reading. Using this free service, authors can make their results available to the community, in citable form, before we publish the edited article. We will replace this *Accepted Manuscript* with the edited and formatted *Advance Article* as soon as it is available.

You can find more information about *Accepted Manuscripts* in the Information for Authors.

Please note that technical editing may introduce minor changes to the text and/or graphics, which may alter content. The journal's standard Terms & Conditions and the Ethical guidelines still apply. In no event shall the Royal Society of Chemistry be held responsible for any errors or omissions in this *Accepted Manuscript* or any consequences arising from the use of any information it contains.

ROYAL SOCIETY OF CHEMISTRY

www.rsc.org/njc

# Citrate Precursor Synthesis and Multifunctional Properties of $YCrO_3$ Nanoparticles

Tokeer Ahmad* and Irfan H. Lone

Nanochemistry Laboratory, Department of Chemistry, Jamia Millia Islamia, New Delhi-110025, India



*Corresponding Author Address:

E-mail address: tahmad3@jmi.ac.in

Phone: 91-11-26981717, Extn: 3261

Fax: 91-11- 26980229

**Abstract:**

Monophasic and highly crystalline $YCrO_3$ nanoparticles with an average grain size of 22 nm and high surface area of 344 $m^2g^{-1}$ have been prepared successfully by using citrate precursor route for the first time. The two band gap values of 1.98 eV and 2.95 eV as obtained may be associated to the transitions of chromium ions. Wedge shaped ferromagnetic loop with saturation magnetization of 2.48 emu $g^{-1}$, remanent magnetization of 0.83 emu $g^{-1}$ and coercive field of 12.78 kOe as well as room temperature ferroelectricity with remanent polarization of 0.009 $\mu C/cm^2$, saturation polarization of 0.026 $\mu C/cm^2$ and coercive field of -0.66 kV/cm establish the multiferroic characteristics in $YCrO_3$ nanoparticles. In addition, humidity sensing characteristic with little repeatability sensor output and the response-recovery time was observed at significance pace.

**Keywords:** Nanoparticles, Orthochromite, Multiferroic, Surface Area, Magnetic and Ferroelectric Properties.

## 1. Introduction:

Metal oxides are widely considered owing to their variety of physical, chemical, and mechanical properties, finding applications in electrical, optical, electrochemical, mechanical, and magnetic devices [1–6]. Attention is being recently paid to develop functional materials that combine more than one property to show diverse effects at nanoscale [7, 8]. In particular, multiferroic materials have attracted tremendous interest in nano-regime because of their potential applications in small electric devices such as electric field induced magnetic memory effects and electro-optic transducer controlled by magnetic fields [9–12]. It has been found that rare earth chromites are known to be p-type semiconductors showing electronic sensitivity like capacitive and resistivity towards humidity and gases such as CO, NO, $N_2O$, $H_2$ etc., which is useful for sensor applications [13-15]. The distorted perovskite structure of orthochromites and the tilting of octahedra have a dramatic effect in physical properties such as ferroelectricity, magnetic order and superconductivity [16]. The dielectric properties and electrical conductivity strongly depend on the size of nanomaterials, surface area, grain boundary, densification, porosity, micro-cracks, etc. These factors contribute strongly to the electrical conductivity and consequently to the ferroelectric response. Hence the P-E hysteresis loops were not found well developed in case of bulk $YCrO_3$ and Pt/$YCrO_3$/Pt thin film capacitor samples due to current leakage problem [17]. It has also been also reported that the $YCrO_3$ compound showing the weak ferromagnetism below 140 K and a ferroelectric transition at 473 K accompanied by hysteresis [18]. However, the origin of the multiferroic existence in orthochromites (like $YCrO_3$) is still a complex subject. Though many reports exist on the synthesis of metal oxide nanoparticles by low temperature methods like reverse micellar method [19, 20], hydrothermal [21], solvothermal [22], polymeric citrate precursor [23] and sonochemical [24] methods. However, little attention has been given

for the formation and nanoscale characterization of pure phase $YCrO_3$ nanoparticles by wet chemical methods. Therefore, the synthesis of such an important material in pure form is of prime significance. Recently, $YMnO_3$ nanoparticles have been reported by polymeric citrate precursor route to obtain the room temperature ferroelectricity [25]. In this paper, we report a facile low-temperature synthesis of $YCrO_3$ nanoparticles using Pechini type citrate precursor synthesis route. As-prepared $YCrO_3$ nanoparticles have been extensively characterized by using the sophisticated techniques and a detailed investigation of the magnetic and electric properties with particular focus on possible multiferroic behavior and humidity sensing properties were also discussed.

## 2. Experimental:

The following chemicals were used in this work: yttrium (III) nitratehexahydrate (Alfa Aesar; 99.9%), chromium (III) nitratenonahydrate (Alfa Aesar; 99.9%), citric acid (Spectrochem; 99%) and ethylene glycol (SD fine-chem Ltd; 99%). All the chemicals were of analytical grade and were used as received without further purification.

The synthesis process implies a mixed solution of citric acid, ethylene glycol and the desired cations to form a gelly type polyester matrix. In this method, water acts as the solvent and the metal ions can be immobilized in a rigid polyester network. The procedure involves use of ethylene glycol: chromium ion: citric acid in the ratio 10: 1: 40. The contents were stirred at room temperature for about 2 h until all the citric acid dissolved and a clear solution was obtained. The stoichiometric amount of aqueous yttrium nitrate was added to this solution and the mixture was further stirred for 2 h until the appearance of green coloured solution. The green solution was stirred at 70$^{o}$C for 2 h. The solution was then kept in an oven at 135$^{o}$C for 20 h to evaporate the solvent and to promote polymerization. The solution turns into the black viscous

resin at this stage. The resin was then charred at 300$^{o}$C for 2 h and then cooled to room temperature. This can greatly reduce the diffusion path lengths of the reactants during the processing [26, 27]. The resin turned into a black mass, which was ground to a powder in an agate mortar. This ground black mass is henceforth referred to as the precursor. Further heating of this precursor results in the formation of the required material with a high degree of homogeneity and dispersion. Hence, green powder of $YCrO_3$ was obtained after heating the precursor at 900$^{o}$C for 12 h.

Powder X-ray diffraction (XRD) studies has been carried out on Bruker D8 Advance X-ray diffractometer with Ni-filtered Cu-Kα radiations of wavelength (λ) = 1.54056 Å. The X-ray diffraction data was recorded in the 2θ range of 20$^{o}$ to 70$^{o}$ with the step size of 0.05$^{o}$ and step time of 1 second. The Kα2 reflections were removed by a stripping procedure to obtain accurate lattice constants. Fourier transform infrared spectra (FT-IR) were recorded on Perkin-Elmer spectrometer (Model 1750). Transmission electron microscopic (TEM) and selected area electron diffraction (SAED) studies have been carried out on FEI Technai $G^2$ 20 TEM with an accelerating voltage of 200 kV. TEM specimens were prepared by taking a small amount of finely ground powder, which was then dispersed in absolute ethanol with the help of ultrasonicator (Model: UP-500 Ultrasonic Processor) and sonicate for about 30 minutes with optimized intensity. A drop from the micropipette of the dispersed sample was placed on a copper grid coated with carbon film. Scanning electron microscopic (SEM) study has been carried out on a new versatile series ZEISS EVO 50 SEM operated at 30 kV acceleration voltage which provides a resolution of 5 nm.

The surface area of the sample was recorded at liquid nitrogen temperature (77 K) using BET surface area analyzer (Model: Nova 2000e, Quantachrome Instruments Limited, USA), by using

'Multipoint BET Method'. Approximately 0.1 g of the powder sample was placed in the sample cell and allowed to degas at one of the degassing station for 3 hours at 250$^{o}$C in a vacuum degassing mode. This removes the contaminants such as water vapour and adsorbed gases from the sample. The degassed sample was then subjected for the analysis and the data was recorded by admitting known quantities of adsorbing nitrogen gas into the sample cell containing the solid adsorbate. As the adsorption occurs, the pressure in the cell changes until equilibrium is reached. From the BET plot, the specific surface area is calculated using the multipoint BET equation. Room temperature optical properties were recorded on an Ocean Optics lambda-25 UV–visible spectrophotometer operating in the reflectance mode. The magnetization studies have been performed using a magnetic property measurement system (MPMS) SQUID magnetometer under an external magnetic field of ±60 kOe at temperatures ranging from 5 to 300 K.

For dielectric, humidity sensing and ferroelectric studies of $YCrO_3$ nanoparticles, a pellet of 8 mm diameter was prepared at a pressure of 5 tons by using 5% PVA solution as binding agent. The pellet was sintered under static air at 1000$^{o}$C for 8 hrs for dielectric and humidity sensing study and for the ferroelectric study the unsintered pellet was used. The pellet was coated with colloidal silver paint (Ted Pella, Inc.) on both the surface and then dry in oven. Dielectric measurements were carried out on HF-LCR meter (6505 P, Wayne Kerr electronics, UK) in the frequency range 100 kHz–1 MHz over a temperature range of 50-400$^{o}$C. The principle of parallel plate capacitor was employed for the evaluation of permittivity. The data acquisition was automated by interfacing the LCR meter with a virtual instrumentation package called LABVIEW (National Instruments). Further, the ferroelectric measurements were carried out on un-sintered pellet at the room temperature under different applied voltages at 50 kHz frequency by using the P-E loop tracer (M/s Radiant Premier II system Instruments, USA). The humidity

sensing characteristic was obtained by the sensor fitted in series with a commercial SHAW dew point meter (model no. SADPTR-R, UK). The desired moist gas concentration was obtained by mixing the commercial dry $N_2$ gas with water vapour at room temperature. The concentration level of moist gas for sensor testing was varied from 2.5 to 25 ppm. The leads of the sensor were connected to an impedance analyzer (Agilent 4294A) for studies.

**3. Results and Discussion:**

**3a. Structural and Morphological Characterization:**

The green powders of $YCrO_3$ nanoparticles have been prepared after heating the black mass precursor at 900$^o$C for further analysis. The powder X-ray diffraction pattern of as-prepared powders is shown in figure 1, in which all the reflections could be indexed satisfactorily in the orthorhombic lattice of $YCrO_3$ (JCPDS : 25-1078). No secondary or impurity peaks from other phases could be detected which confirms the monophasic nature of multiferroic $YCrO_3$. The reasonably high intensity and appearance of distinct reflections may be attributed to the well crystallinity in the as-prepared multiferroic nanoparticles. The average crystallite size was determined to be 34 nm using X-ray line broadening studies on (121) reflection by applying the Scherrer's formula.

Fig. 2 (a, b) shows the FTIR spectra of the powder before and after calcination at 800$^o$C. Numbers of absorption peaks were observed originating from organic phases in the ground powder before calcination. However, in the spectrum of the calcined powder, all such peaks were disappeared. The simultaneous disappearance of peaks from the band at 3434.3 cm$^{-1}$ to 1254.9 cm$^{-1}$ and appearance of new peaks at 616 cm$^{-1}$, 493.1 cm$^{-1}$, 440 cm$^{-1}$ and 373.5 cm$^{-1}$ for the calcined sample at 800$^o$C, indicated the formation of $YCrO_3$ nanoparticles as shown in fig. 2b. The band around 3434.3 cm$^{-1}$ of the precursor heated at 300$^o$C shown in fig. 2a is assigned to the

stretching of surface hydroxyls originating from the dissociative chemisorption of water. Esterification between citric acid and ethylene glycol before calcination is confirmed by the presence of the 1716 and 1254.9 $cm^{-1}$ bands assigned to the C=O and C-O-C stretching vibrations for the ester group, respectively [28].

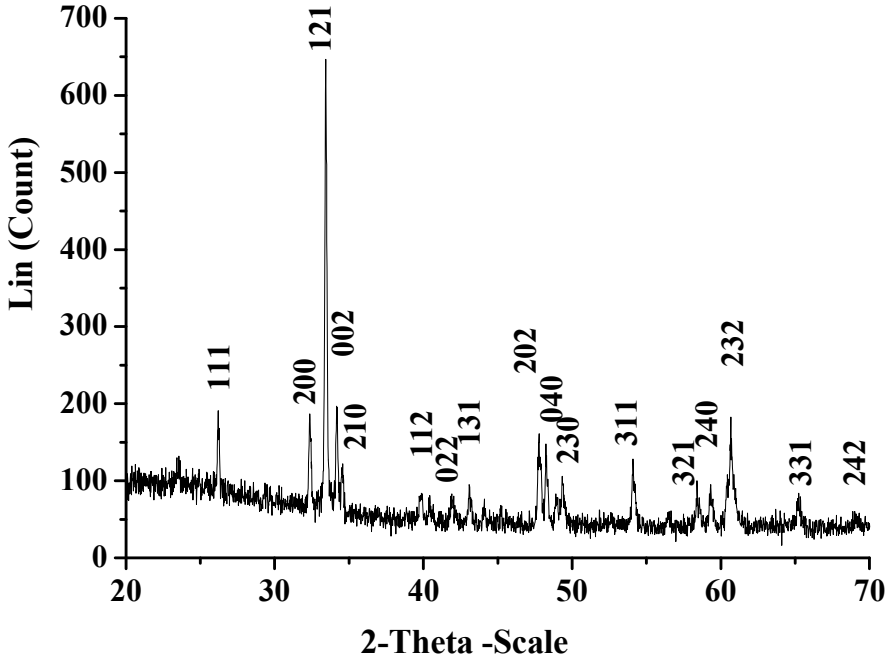


**Figure 1.** Power X-ray diffraction pattern of $YCrO_3$ nanoparticles.

The formation of ester formation was further confirmed by the band centered at 1551.4 $cm^{-1}$ of the carboxylate ($-COO^-$) group. Chromium oxide peaks generally reveal the absorption bands below 1000 $cm^{-1}$ due to inter-atomic vibrations [29]. The formation of $YCrO_3$ heated after 800$^oC$ was confirmed by the appearance of sharp peaks at 616, 493.4 and 440 $cm^{-1}$ as shown in fig. 2b, which corresponds to Cr–O stretching, Y–O stretching and O–Cr–O deformation vibration, respectively [30].

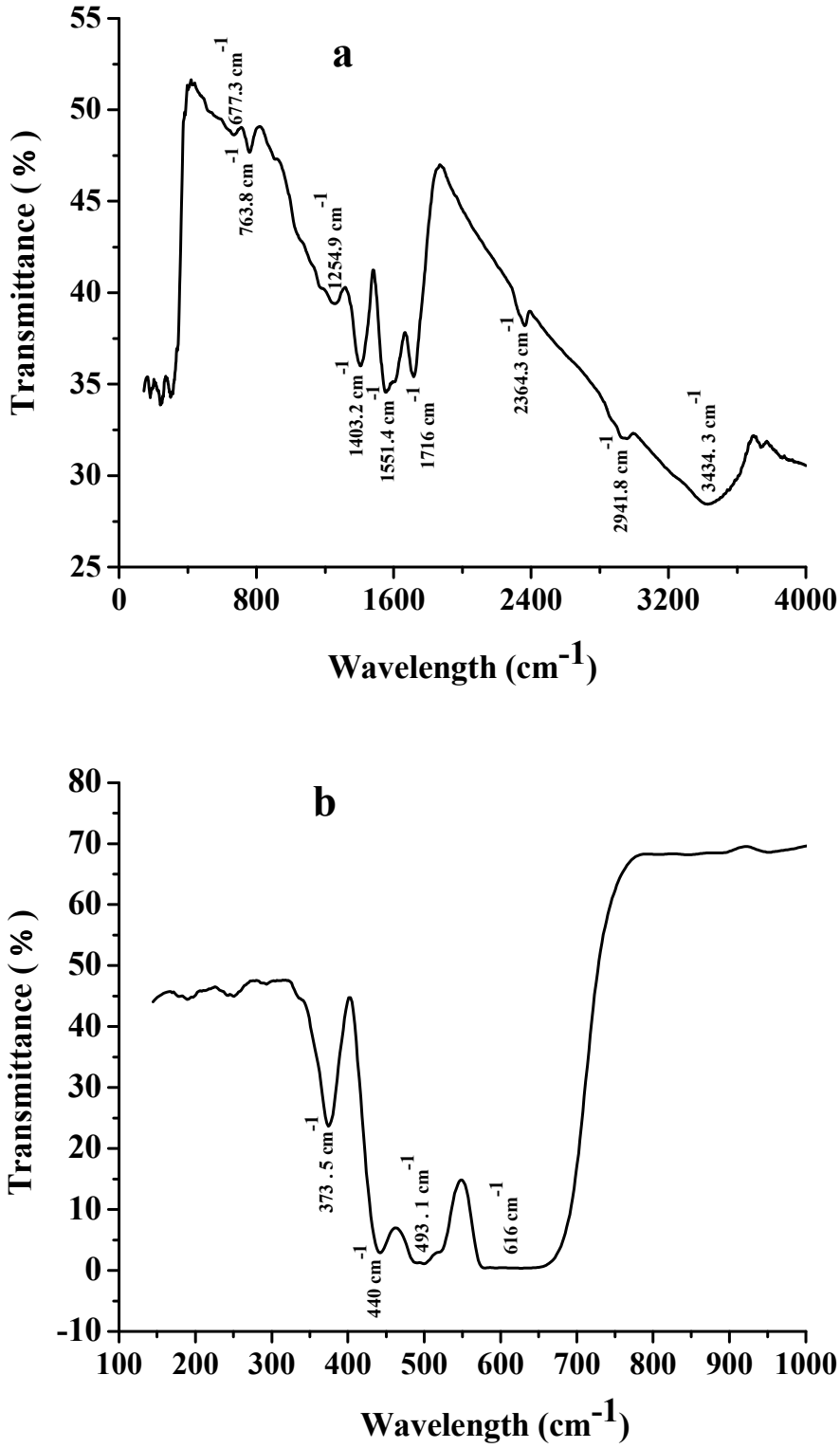


**Figure 2.** FTIR spectra of $YCrO_3$ nanoparticles (a) before calcination and (b) after calcination at 900$^{o}$C.

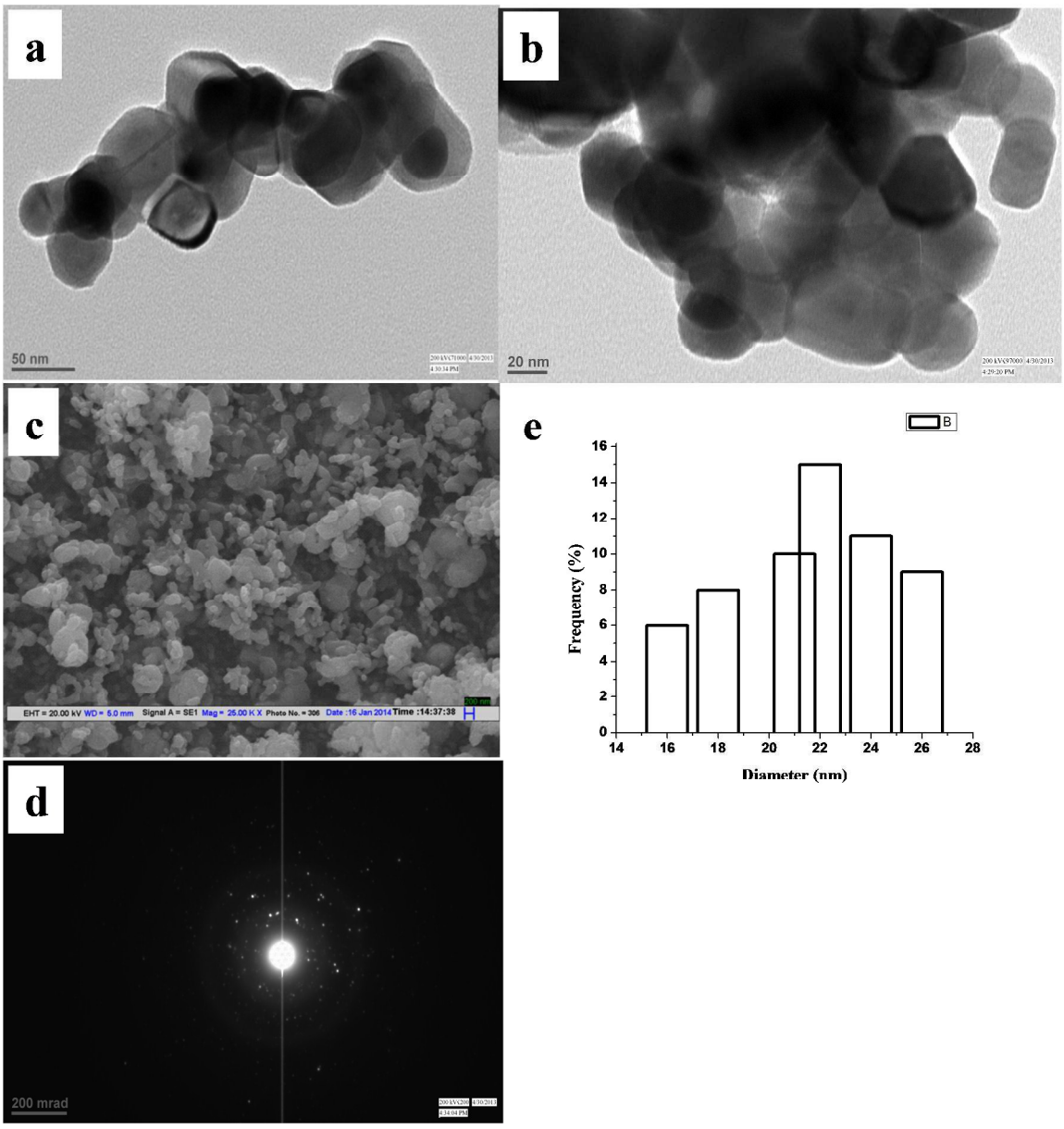


**Figure 3.** (a, b) TEM , (c) SEM, (d) SAED images and (e) size distribution histogram of $YCrO_3$ nanoparticles.

The estimation of the average particle size of $YCrO_3$ nanoparticles was carried out by using TEM and SEM studies as shown in fig. 3, which shows the particles lies in the size range of 15-30 nm with an average grain size of 22 nm. It has also been observed from the lower

amplification TEM image in fig. 3 b that the nano particles are well-dispersed, uniformly distributed with hexagonal in shape and slightly less agglomerated. Fig. 3d is the selected-area electron diffraction (SAED) pattern of $YCrO_3$ nanoparticles and the sharp diffraction spots indicate the well-developed nano-crystalline structure. The rings with different diameters in the pattern are duly assigned to the different lattice planes of the $YCrO_3$ nanoparticles and were found in agreement with the XRD studies. The size distribution histogram (fig. 3 e) clearly shows the statistical average grain size of 21.1 nm and the standard deviation was calculated by using the formula

$$\sigma = \sqrt{\sum_{i=xi}^{n} (xi - \mu)^2}$$

By using the data values of the histogram the variance was found 11.47 and square root of the variance called standard deviation which was found to be 3.38.

**3b. Surface Area and UV-visible Spectroscopic Studies:**

The Brunauer-Emmett-Teller (BET) gas adsorption method has become the most widely used standard procedure for the determination of the surface area of finely divided porous materials. Fig. 4a shows the BET plot of $YCrO_3$ nanoparticles which gives the highest surface area of 344 $m^2g^{-1}$. The pore characteristics of as-prepared nanoparticles have been determined using DA (Dubininz-Astakhov) and BJH (Barrett-Joyner-Halenda) methods. The BJH pore size distribution curves confirmed the predominance of mesopores of pore radius of 16.1 Å (fig. 4b), however, DA plot displayed the pore radius of 15 Å for $YCrO_3$ nanoparticles as shown in fig. 4c. The nitrogen adsorption isotherm of $YCrO_3$ powders is shown in the inset of fig. 4b which ascribed the type-IV isotherm indicates the presence of mesopores nature [31]. The positive BET

constant 'c' value (2.95) using BET plot was associated to the high affinity and high heat of adsorption of $YCrO_3$ nanoparticles with the adsorbate gas.

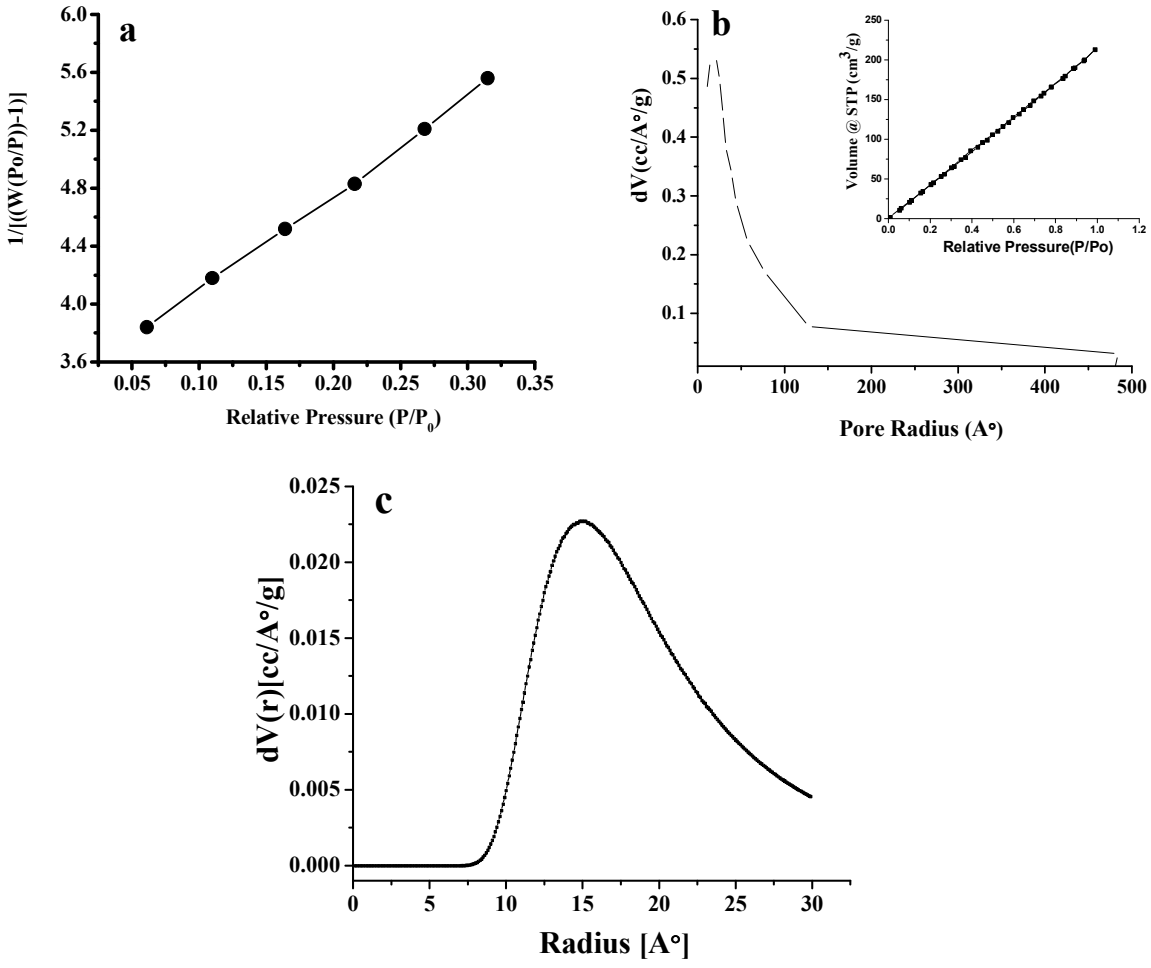


**Figure 4.** (a) BET plot, (b) BJH and (c) DA pore size distribution plots of as-prepared $YCrO_3$ nanoparticles. Inset of (b) is the $N_2$ adsorption desorption isotherm.

Fig.5a shows the UV-visible diffuse reflectance spectra and fig. 5b is the band gap plot (inset shows energy level diagram of the $Cr^{3+}$ ions) of $YCrO_3$ nanoparticles. It can be seen that the $YCrO_3$ nanoparticles have two absorption edges present at about 460 nm and 610 nm, respectively which may be due to the typical d–d transitions of $Cr^{3+}$ ($d^3$) system with the parity-

forbidden and spin-allowed transitions from the ground level $^4A_{2g}$ (4F) to $^4T_{2g}$ (4F) and $^4T_{1g}$ (4F) [$^4T_{1a}$], respectively. Minor bands, because of the parity and spin forbidden transitions from $^4A_{2g}$ (4F) to $^2E_g$ (2G) and $^2T_{1g}$ (2G), are observed at approximately 730 nm and 691 nm, respectively [32]. The optical band gap was determined using the Tauc's formula [33] by applying the Kubelka-Munk (KM) function $F(R)=\frac{(1-R)^n}{2R}$, where R is the reflectance and Eg is the energy band gap in electron volts. Exponent 'n' depends on the type of transition and it may have values 1/2, 2, 3/2 and 3 corresponding to the allowed direct, allowed indirect, forbidden direct and forbidden indirect transitions respectively. In the present case, the best fit of $F(R)^n$ versus photon energy (Eg) was obtained for n = 1/2. Thus, the $E_g$ values were determined by extrapolating the linear portion of the $F(R)^{1/2}$ versus Eg plot (Figure 5b). The two band gap values of 1.98 eV and 2.95 eV were found that may correspond to the transitions of chromium ion from the ground level [32]. Secondary edges were also found that can be assigned to crystal field transitions and has been observed at higher wavelengths.

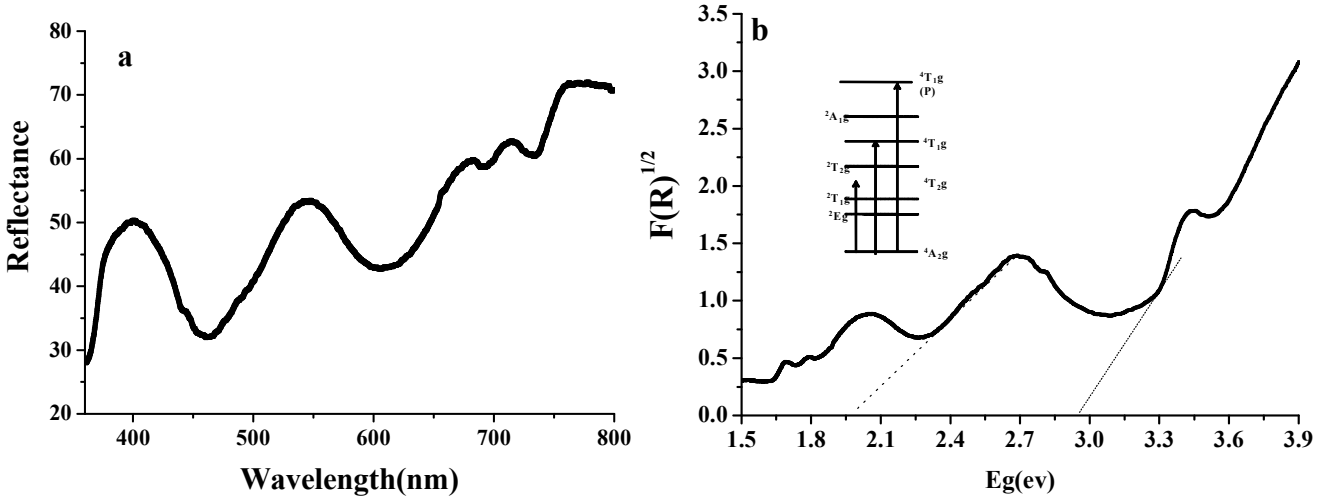


**Figure 5.** (a) UV-visible reflectance spectra and (b) band gap plot and inset shows the energy level diagram of $Cr^{3+}$ ions in $YCrO_3$.

**3c. Magnetic Properties:**

The temperature dependence of magnetization of $YCrO_3$ nanoparticles have been studied under an external magnetic field of ±60 kOe in the temperature range of 5 to 300 K. Fig.6 (a) shows the molar magnetic susceptibility of $YCrO_3$ nanoparticles measured as a function of temperature at a constant magnetic field (1 kOe). The sample molar magnetic susceptibility ($\chi_M$) decreases with increasing temperature in the range 5-300 K. A sharp ferromagnetic (FM)-like transition can be found around 100 K, which was supported by the magnetic hysteresis loop at 5 K. This ferromagnetic ordering temperature at 100 K was slightly lower than the earlier report [8] and the Neel temperature ($T_N \sim 120$ K) of this study was also found lower than earlier studies [17, 34]. In order to investigate further the magnetic properties, the Curie-Weiss equation was fitted by using the following relation, $\chi = \frac{C}{T - \theta_p}$, where $\chi$ is the magnetic susceptibility, $\chi^{-1}$ is the inverse magnetic susceptibility, C is the curie constant and $\theta_p$ is the Weiss temperature [35]. According to the Curie-Weiss law, the temperature (T) dependence of inverse susceptibility ($\chi^{-1}$) was fitted with a negative extrapolated temperature ($\theta_p$ = -250 K) as shown in fig. 6a, implying the antiferromagnetic interaction which was lower than previous report and it may be due to the nanocrystalline nature [36]. Fig. 6 (b) displays the M-H plot at 5 K temperature which describes the wedge shaped ferromagnetic hysteresis loop with the saturation magnetization of 2.48 emu $g^{-1}$), remanent magnetization of 0.83 emu $g^{-1}$ and coercive field of 12.78 kOe for $YCrO_3$ nanoparticles. These parameters were found much better as compared to earlier reports [18, 36]. Bulk $YCrO_3$ generally possess antiferromagnetic interactions but in the nanoregime each particle behaves as a nano-domain with independent spins fluctuating with respect to temperature. The presence of weak ferromagnetism in as-prepared $YCrO_3$ nanoparticles could be attributed to the

canting of spins and associated to the D-M (Dzyaloshinskii-Moriya) interactions in chromites [37, 38].

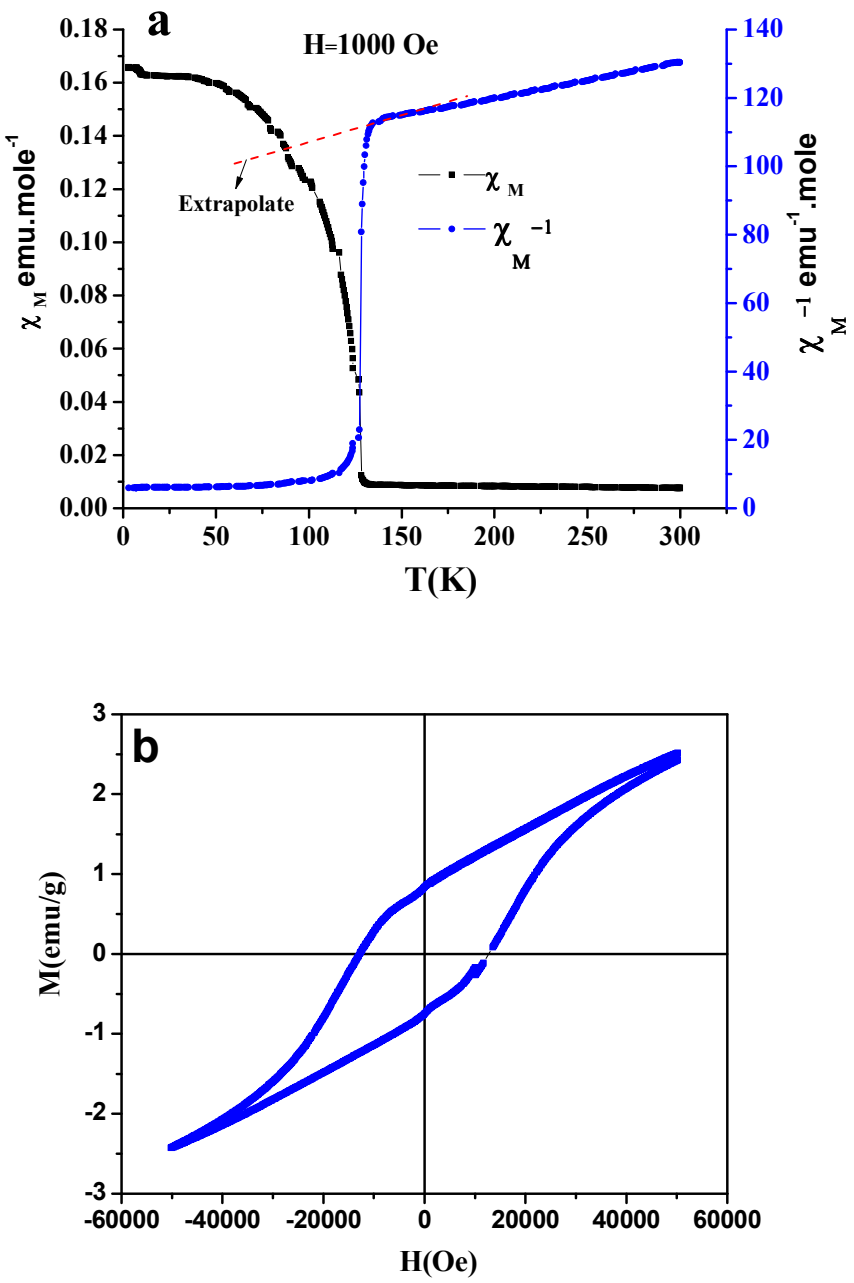


**Figure 6.** (a) Temperature dependence of susceptibility at 1 kOe and (b) M-H curve of $YCrO_3$ nanoparticles.

Rare earth chromites such as $YCrO_3$ and $GdCrO_3$ are typically perovskite type compounds and stabilize in an orthorhombic distorted structure. Therefore the oxygen forming polyhedral around chromium is distorted which results the ferroelectricity and the (Cr-O-Cr) apical bond is reduced from $180^o$ giving the antiferromagnetic ordering in $YCrO_3$ system [39, 40]. In addition, numerous reports claim the change in the ferroic ordering due to size effects in different structures which were observed through measurement of both Néel temperature as well as Curie temperature at reduced dimensions [41, 42].

**3d. Electrical Properties:**

Polarization-electric field (P-E) hysteresis studies of polycrystalline $YCrO_3$ nanoparticles at different applied voltages of 200-400 V are shown in fig. 7 and the measurements were performed at 50 kHz. The ferroelectric hysteresis loop of $YCrO_3$ nanoparticles was difficult to obtain at high temperature due to the leakage current. Hence the unsintered pellet was used for the study of ferroelectric property. The room temperature ferroelectric loop of $YCrO_3$ nanoparticles was obtained with remanent polarization ($P_r$) of 0.009 $\mu C/cm^2$, saturation polarization ($P_s$) of 0.026 $\mu C/cm^2$ and coercive field ($E_c$) of -0.66 kV/cm at 400 V. The obtained results like ferroelectric loop and data values of $YCrO_3$ nanoparticles were found better than the earlier reported values [17]. The origin of ferroelectricity in $YCrO_3$ nanoparticles was explained by Rao et al. and showed that the non-centrosymmetry in $YCrO_3$ is local in nature [43]. Local fluctuations within the sample can lead to the creation of nanosized polar region which in turn leads to the creation of dipoles similar to the frustrated ferroelectrics [44, 45]. The ferroelectric loop of $YCrO_3$ nanoparticles strongly dependent on the applied electric field, which may led to its potential application in nonvolatile multistate memory devices.

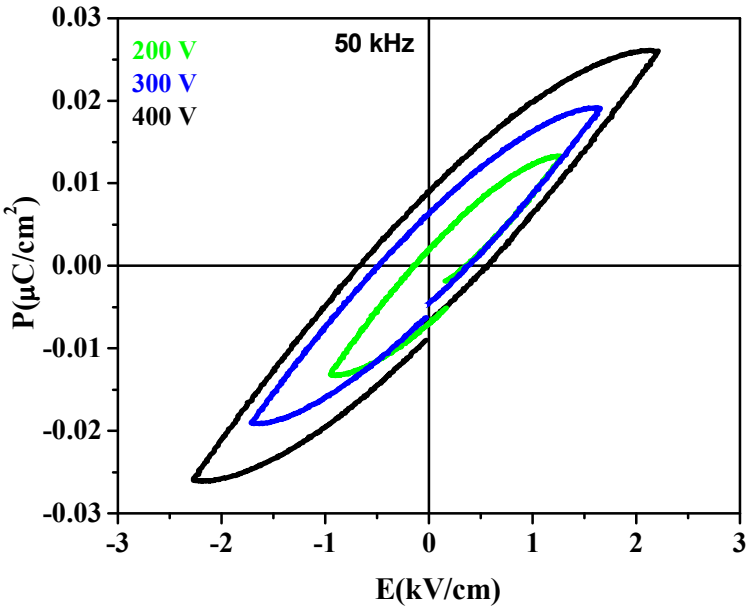


**Figure 7.** P-E loop studies of nanocrystalline $YCrO_3$ at various applied electric fields.

The dielectric properties of $YCrO_3$ nanoparticles were measured on HFLCR meter as a function of frequency and temperature as shown in fig. 8. The dielectric constant ($\varepsilon$) decreases significantly with increasing frequency, and two dielectric anomalies were found between the temperature ranges of 50°C to 400°C. Previous results of $YCrO_3$ showed the dielectric anomaly at 177°C in the temperature ranges of 27°C to 247°C [31]. However, in present study, the temperature range of dielectric constant was further extended up to 400°C and hence two peak maxima at 109°C and 370°C temperatures were found. It seems that the sample might be a relaxor, and therefore, these anomalies could be related to the ferroelectric phase transitions at these particular temperatures. Both these anomalies were further characterized at different frequencies, which show that the increase in frequency leads to the distinction of anomalies. The dielectric constant and dielectric loss decreases with increase in frequency at room temperature (fig. 8 b) which may be due to failure of electric dipoles to follow the alternating applied field that can be explained on the basis of Maxwell–Wagner interfacial polarization [46, 47]. The high

value of dielectric constant of $YCrO_3$ nanoparticles may be due to the high surface area as compared to the bulk phase. This might be associated to the fact that more charges get accumulated at the surface thereby increases the polarization of the nano-material.

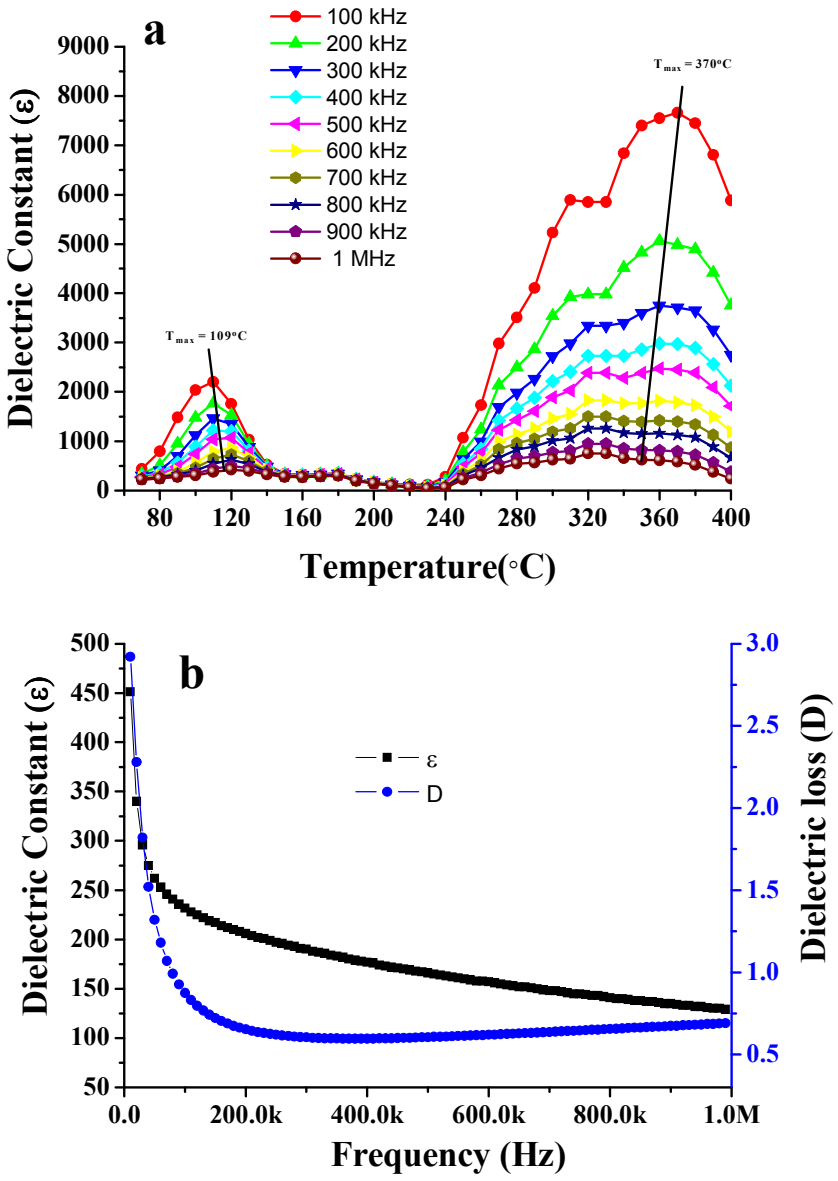


**Figure 8.** (a) Temperature dependence of dielectric constant at different frequencies and (b) shows the variation of dielectric constant and dielectric loss as a function of frequency at room temperature of $YCrO_3$ nanoparticles.

Electrical impedance measurement is a powerful tool to investigate the movement and reactions of charged species in an electrochemical cell [48]. The ac conductivity versus temperature plot of $YCrO_3$ nanoparticles at different frequencies is shown in fig. 9 (a). It has been observed that conductivity linearly increases with the increase in temperature and reached the maximum value at 370$^o$C, and there after decreases. With the increase in frequency, the value of conductivity slightly increases, this marginal change has been shown in the inset of fig. 9 (a). The change of conductance and impedance with frequency at room temperature were shown in fig. 9 (b). The conductance varies linearly with the increase in frequency; however, the impedance has an inverse effect at room temperature. The total impedance consists of a resistive, a capacitive and an inductive component and is therefore linearly decreases with the frequency of the probe signal. At low frequency range, the ac conductivity is nearly independent of the frequency and has been attributed to the dc conductivity of the sample. The dc conductivity ($\sigma_{dc}$) is plotted as the function of reciprocal temperature as shown in fig.10 and it well obeys the Arrhenius relation. $\sigma = \sigma_0 \exp(-\frac{E_{cond}}{k_B T})$, where $\sigma_o$ is the pre-exponential term and $E_{cond}$ is the conduction activation energy. The activation energy ($E_{cond}$) was calculated from the plot of $\log\sigma_{dc}$ vs. 1000 / T (K) plot and found to be 0.14 eV, which means that the ionic charges and grain boundary defects are the carriers of the thermal conductivity and may also related to the point defects in semi-conductive ferroelectric materials [49].

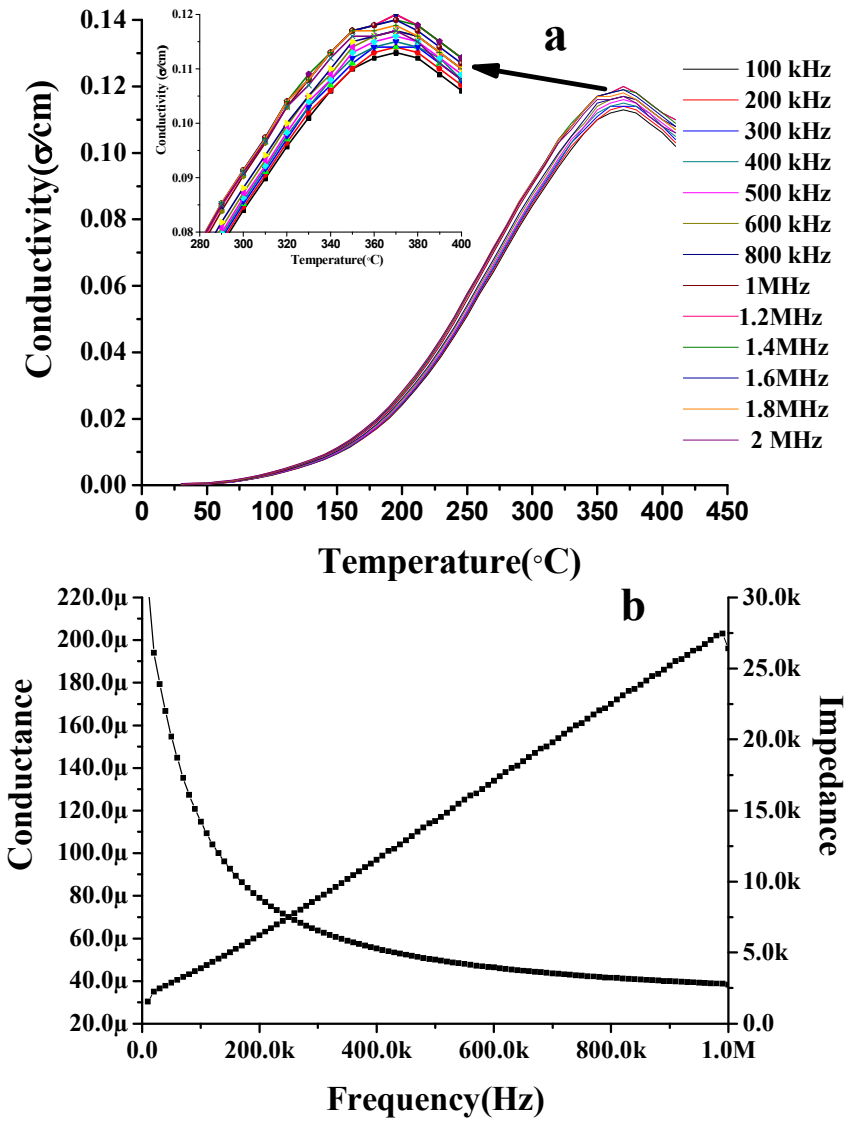


**Figure 9.** (a) Variation of ac conductivity with temperature at different frequencies and (b) linear change of conductance and impedance with frequency at room temperature.

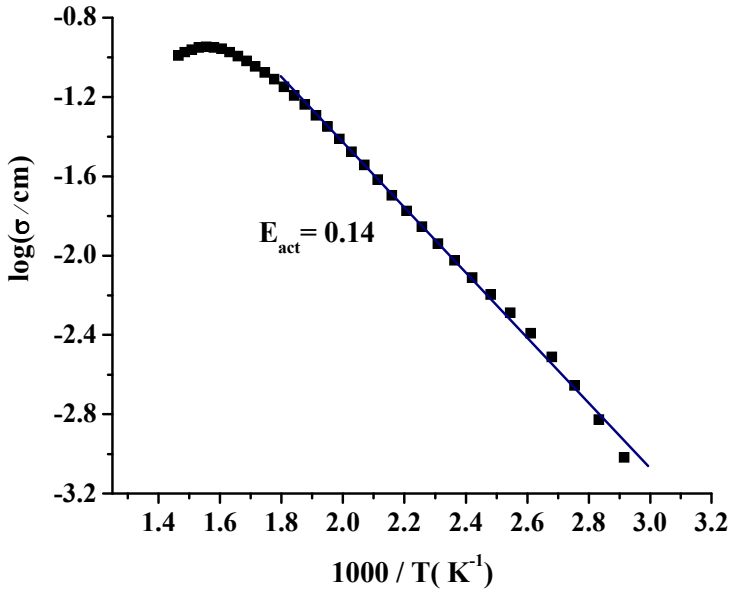


**Figure 10.** Arrhenius plot of $YcrO_3$ nanoparticles. The symbols are experimental points and the solid line is Arrhenius fit.

**3e. Humidity Sensing Properties:**

The capacitance and dissipation factor have been measured with relative humidity at 1 kHz as shown in fig. 11 (a). The magnitude of the dissipation factor is very small which indicates that the content of moisture in the pellet is very small. The capacitance value increases with increase in moisture. When the sensor exposed to moisture is excited by AC signal with certain frequency, the water molecules are polarized. The polar water molecules try to orient in the positive direction of the field and then reorient in the negative direction of the field and has been manifested that the dielectric constant and capacitance will increase with water adsorption. To observe the orientation loss of moisture adsorbed by the thin dielectric layer, the dissipation factors are determined at different moisture level. Since the capacitive sensor for moisture detection is made lossy, the phase shift will increase with increase in moisture concentration. The repeatability of the sensor at the same moisture level for several moisture cycles is shown in fig.

11 (b). There exists little repeatability sensor output and the response- recovery times of the sensor are occurring at the significance pace. This may be due to the absorption and desorption of water molecules and they do not take place at the similar rate. Thus the sensor takes more time to desorp the water molecules from nano order pores. Hence, in between two peak cycles, there exist small anomalies that is slightly discouraging indication for normal sensor.

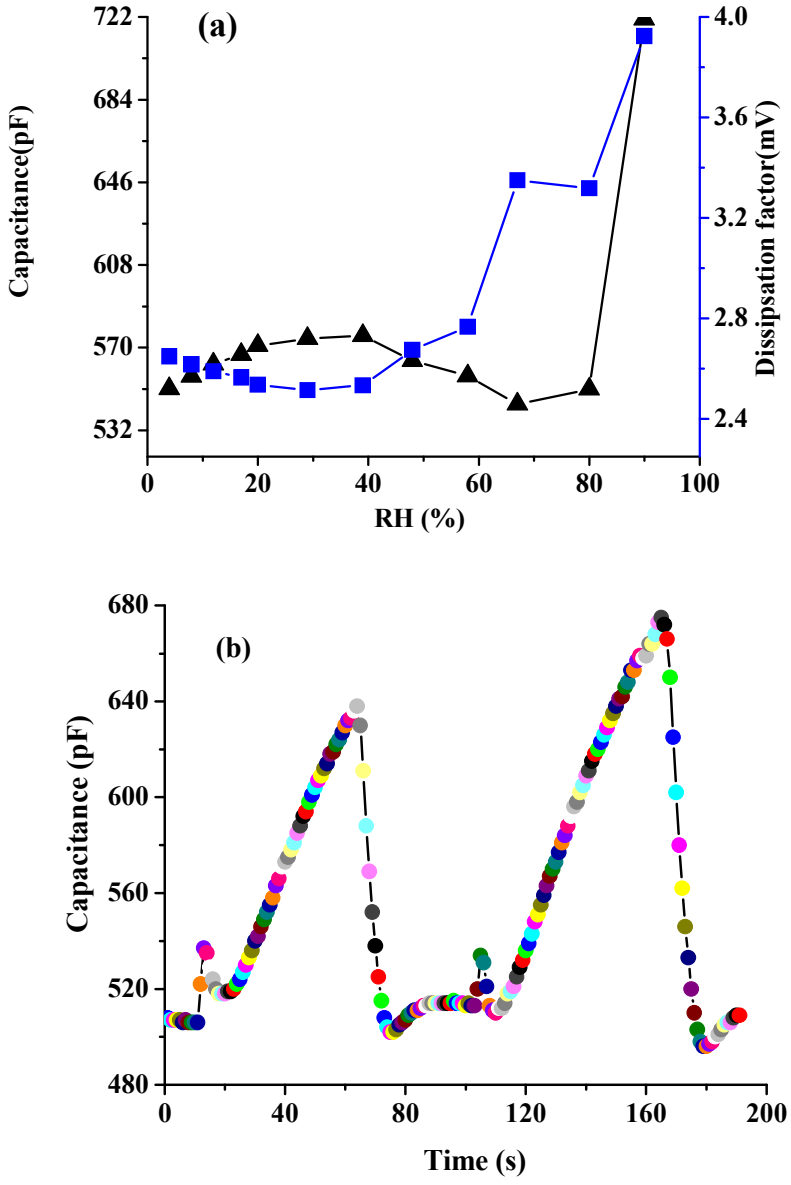


**Figure 11.** (a) The variation of capacitance and dissipation factor with relative humidity and (b) is the repeatability plot of $YCrO_3$ nanoparticles.

## 4. Conclusion:

We have successfully synthesized multiferroic $YCrO_3$ nanoparticles with high surface area (344 $m^2g^{-1}$) by using metal organic precursor method for the first time. PXRD and FTIR studies showed that the as-prepared nanoparticles are highly crystalline and monophasic with orthorhombic structure. The microscopic techniques (TEM/SEM) and SAED images showed that the as-prepared $YCrO_3$ nanoparticles have high homogeneity and fine grain morphology with average grain size 22 nm. Reflectance measurements showed the optical energy band gap lies in the visible range for as- prepared $YCrO_3$ nanoparticles. Wedge shaped ferromagnetic hysteresis and room temperature ferroelectric loop confirm the multiferroic nature of $YCrO_3$. The dielectric properties as a function of temperature and frequency were established in $YCrO_3$ nanoparticles, with addition of conductivity and impedance. Lastly, humidity sensing properties of $YCrO_3$ has been studied, where we find significant repeatability of the $YCrO_3$ sensor at the same moisture level for several moisture cycles with little repeatability sensor output. These results illuminate a promising potential to apply this material in memory devices that can be addressed both electrically and magnetically.

## 5. Acknowledgements:

This work is financially supported by Innovative Research Activities of Jamia Millia Islamia, New Delhi (AC-6(15)/RO/2014). Authors thank AIIMS New Delhi for electron microscopic studies and Prof. K. V. Ramanujachary (Rowan University, USA) for carrying out the magnetic measurements. We also acknowledge Dr. V. R. Reddy (UGC-DAE Indore) for P-E measurements. IHL specially thanks to University Grant commission (UGC) New Delhi for the grant of JRF and SRF.

**6. References:**


[1] M. Niederberger and N. Pinna, *Springer, Dordrecht*, 2009.

[2] C. Kumar, *Wiley-VCH, Germany*, 2009.

[3] S. K. Mandal, T. Rakshit, S. K. Ray, S. K. Mishra, P. S. R. Krishna and A. Chandra, *J. Phys. Condens. Matter*, 2013, **25**, 055303.

[4] H. F. Dong, Z. G. Wu, S. Y. Wang, W. H. Duan and J. B. Li, *Appl. Phys. Lett.,* 2013, **102**, 072905.

[5] J. Kiser, P. Finkel, J. Q. Gao, C. Dolabdjian, J. F. Li and D. Viehland, *Appl. Phys. Lett.,* 2013, **102**, 042909.

[6] E. J. Guo, K. Deorr and A. Herklotz, *Appl. Phys. Lett.,* 2012, **101**, 242908.

[7] D. Li, W. Y. Teoh, C. Selomulya, R. C. Woodward, P. Munroed, and R. Amal, *J. Mater. Chem.,* 2007, **17**, 4876.

[8] V. Bedekar, R. Shukla and A. K. Tyagi, *Nanotechnology* 2007, **18**, 155706.

[9] N. A Hill, *J. Phys. Chem. B.,* 2000, **104**, 6694.

[10] N. Hur, S. Park, P. A. Sharma, J. A. Ahn, S. Guha and S. W. Cheong, *Nature* 2004, **429**, 392.

[11] W. M. Zhu and Z. G. Ye, *Ceram Int.* 2004, **30**, 1435.

[12] R. Seshadri and N. A. Hill, *Chem. Mater*., 2001, **13**, 2892.

[13] M. Siemons and U. Simon, Sens. Actuators, B, 2007, **126**, 181.

[14] N. Russo, D. Mescia, D. Fino, G. Saracco and V. Specchia, *Ind. Eng. Chem. Res.,* 2007, **46**, 42.

[15] D. Lakshmi and R. Sundaram, *Sens. Transducers J.,* 2008, **97**, 74.

[16] T. Wolfram and S. Ellialtioglu, (*Cambridge: Cambridge University Press*), 2006, p 246.

[17] Z. X. Cheng, X. L. Wang, S. X. Dou, H. Kimura and K. Ozawa, *J. Appl. Phys.,* 2010, **107**, 09D905(1-3).

[18] C. R. Serrao, A. K. Kundu, S. B. Krupanidhi, U. V. Waghmare and C. N. R. Rao, *Phys. Rev. B*, 2005, **72**, 220101.

[19] A. Ganguly, P. Tring, K. V. Ramanujachary, T. Ahmad, A. Mugweru and A. K. Ganguli, *J. Colloid Interface Sci.,* 2011, **353**, 137.

[20] A. K. Ganguli, S. Vaidya and T. Ahmad, *Bull. Mater. Sci.* 2008, **31(3)**, 415.

[21] A. Ganguly, T. Ahmad and A. K. Ganguli, *Langmuir,* 2010, **26**, 14901.

[22] T. Ahmad, S. Khatoon, K. Coolahan and S. E. Lofland, *J. Alloy Compd.* 2013, **558**, 117.

[23] T. Ahmad, I. H. Lone, M. Ubaidullah and K. Coolhan, *Mater. Res. Bull.,* 2013, **48**, 4723.

[24] T. Ahmad, I. A. Wani, O. A. Al-Hartomy, A. S. Al-Shihri and A. Kalam, *J. Mol. Struct.* 2015, **1084**, 9.

[25] T. Ahmad, I. H. Lone and M. Ubaidullah, *RSC Adv.* 2015, **5**, 58065.

[26] G. A. Bowmaker, *Chem. Commun;* 2013, **49**, 334.

[27] G. A. Bowmaker, J. V. Hanna, R. D. Hart, B. W. Skelton and A. H. White, *Dalton Trans;* 2008, 5290.

[28] L. J. Bellamy, *2nd Ed., London, England*, 1958.

[29] F. Farzaneh and M. Najafi, *J. Sci. Islam. Repub. Iran*, 2011, **22**, 329.

[30] D. S. Patil, N. Venkatramani and V. K. Rohatgi, *J. Mater. Sci. Lett.,* 1988, 7, 413.

[31] S. Brunauer and D. Teller, *J. Am. Chem. Soc.,* 1940, **62**, 1723.

[32] R. S. Pavlov, V. B. Marza and J. B. Carda, *J. Mater. Chem.,* 2002, **12**, 2825.

[33] J. Tauc, *Plenum Press, New York*, 1974.

[34] B. Tiwari, M. K. Surendra and M. S. R. Rao, *J. Phys. Condens. Matter*, 2013, **25**, 216004.

[35] A. H. Morish*, IEEE Press, New York*, 2001.

[36] A. Duran, A. M. Arevalo-Lopez, E. Castillo-Martınez, M. Garcıa-Guaderrama, E. Moran, M. P. Cruz, F. Fernandez and M. A. Alario-Franco, *J. Solid State Chem.,* 2010, **183**, 1863.

[37] B. C. Tofield, B. E. F. Fender, *J. Phys. Chem. Solids* 1970, **31**, 2741.

[38] V. E. Dmitrienko, E. N. Ovchinnikova, S. P. Collins, G. Nisbet, G. Beutier, Y. O. Kvashnin, V. V. Mazurenko, A. I. Lichtenstein and M. I. Katsnelson, *Nature Physics* 2014, **10**, 202.

[39] T. Wolfram and S. Ellialtioglu, *Electronic and Optical Properties of d-Band Perovskites, Cambridge University Press, Cambridge*, 2006, 246.

[40] R. D. Shannon, *Acta Crystallogr. A*, 1976, **32**, 751.

[41] S. M. Selbach, T. Tybell, M. A. Einarsrud and T. Grande, *Chem. Mater.* 2007, **19**, 6478.

[42] L. Sun, P. C. Searson and C. L. Chien, *Phys. Rev. B* 2000, **61**, 6463.

[43] C. N. R. Rao and C. R. Serrao, *J. Mater. Chem.,* 2007, **17**, 4931.

[44] R. Ranjan, R. Hackl, A. Chandra, E. S. D. Trots and H. Boysen, *Phys. Rev. B* 2007, **76**, 224109.

[45] I. Singh, A. K. Nigam, K. Landfester, R. Munoz-Espi and A. Chandra, *Appl. Phys. Lett.,* 2013, **103**, 182902.

[46] K. W. Wagner, *Ann. Phys.* 1913, **40**, 817.

[47] C. G. Koops, *Phys. Rev.* 1951, **83**, 121.

[48] E. Barsoukov and J. R. Macdonald, *John Wiley & Sons, New Jersey*, 2005, 264.

[49] O. Raymond, R. Font, N. Suarez-Almodovar, J. Portelles, and J. M. Siqueiros, *J. Appl. Phys.,* 2005, **97**, 084107.

**Graphical abstract:**

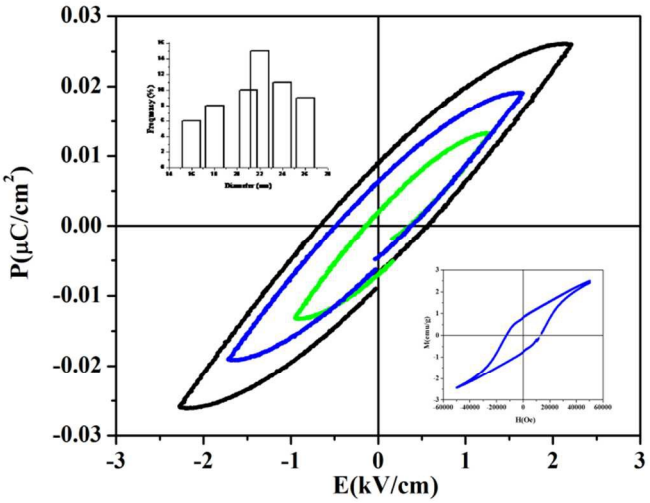


Monophasic and multifunctional $YCrO_3$ nanoparticles (22 nm) with high surface area of 344 $m^2g^{-1}$ exhibit the well defined multiferroic characteristics.